BAYESIAN DATA FUSION AND INVERSION IN X-RAY MULTI-ENERGY COMPUTED TOMOGRAPHY

Caifang Cai [*], *Ali Mohammad-Djafari* [†], *Samuel Legoupil* [‡], *and Thomas Rodet* [§]

CNRS, SUPELEC, UNIV PARIS SUD, L2S, 3 rue Joliot-Curie, 91192 Gif s/Yvette, France
CEA, LIST, DISC, LITT, 91191 Gif s/Yvette, France

ABSTRACT

In this paper, we first introduce a *Multi-Energy Computed Tomography* (MECT) forward projection model based on the base material decomposition method. In this method, an object is considered into a linear combination of the fractions of several base materials weighted by X-ray beam energy functions. Then, three different data fusion inversion approaches are proposed to reconstruct the base material fractions. For the first pre-separation reconstruction approach, the base material decomposition is carried on in the projection space while in the second post-separation approach, the base material decomposition is carried on the attenuation coefficients. The third approach is a joint Bayesian inversion method. Finally, the reconstruction performances of the three reconstruction methods are compared on the simulated data.

Keywords: X-ray, Multi-Energy Computed Tomography, Inverse problem, Bayesian estimation.

1. INTRODUCTION

The classical X-ray *Computed Tomography* (CT) uses a single acquisition spectrum to reconstruct the attenuation property of the object. MECT system shows its outstanding advantages comparing to the classic monochromatic CT system as it is able to reconstruct other characteristics of the object otherwise than the attenuation, such as the base material fractions [1], the effective atomic number and the mass density [2]. On the other hand, as a result of the employment of multiple acquisition X-ray beam energies, the reconstruction problem becomes intractable, which also limits its applications. So far, only dual energy CT system is in use.

1.1. Energy selective Radon transform

Given beam energy ε, the Radon transform describes the relation between the *Linear Attenuation Coefficient* (LAC) $\mu(\boldsymbol{r}, \varepsilon)$ and the sinogram $p(\boldsymbol{s}, \theta, \varepsilon)$.

$$p(\boldsymbol{s}, \theta, \varepsilon) = \int_{l_s(\theta)} \mu(\boldsymbol{r}, \varepsilon) dl \tag{1}$$

where$\boldsymbol{r}$ is the Cartesian coordinate, $\boldsymbol{r} = (x, y)$ in 2D and $\boldsymbol{r} = (x, y, z)$ in 3D. $\boldsymbol{s}$ is the coordinate in the sinogram space and θ is the projection angle, $l_s(\theta)$ is the X-ray beam trace in the object at the projection angle θ. $\mu(\boldsymbol{r}, \varepsilon)$ is the LAC of the object at energy ε.

As we see the LAC $\mu(\boldsymbol{r}, \varepsilon)$ depends both on the material and the energy. We suppose it to be separable and it can be written as:

$$\mu(\boldsymbol{r}, \varepsilon) = \sum_{i}^{n_f} a_i(\varepsilon) x_i(\boldsymbol{r}) \tag{2}$$

where n_f is the number of decomposition functions. In the following discussion $n_f = 2$. $x_i(\boldsymbol{r})$ is the material based decomposition function, $a_i(\varepsilon)$ is the energy based decomposition function. The projection becomes the linear combination of sinograms of the material based decompositions weighted by the energy functions:

$$p(\boldsymbol{s}, \theta, \varepsilon) = a_1(\varepsilon) q_1(\boldsymbol{s}, \theta) + a_2(\varepsilon) q_2(\boldsymbol{s}, \theta) \tag{3}$$

where the sinograms $q_1(\boldsymbol{s}, \theta)$, $q_2(\boldsymbol{s}, \theta)$ are the Radon transform of $x_1(\boldsymbol{r})$ and $x_2(\boldsymbol{r})$ separately.

$$q_1(\boldsymbol{s}, \theta) = \int_{l_s(\theta)} x_1(\boldsymbol{r}) dl \tag{4a}$$

$$q_2(\boldsymbol{s}, \theta) = \int_{l_s(\theta)} x_2(\boldsymbol{r}) dl \tag{4b}$$

2. FORWARD MODEL

2.1. Parametrization

In our forward model, we suppose that the attenuation of the materials contained in the object can be estimated by the linear combination of several basic materials. This has been justified in medical applications with water and bone as the two basic materials [3]. So the energy based decomposition functions $a_1(\varepsilon)$ and $a_2(\varepsilon)$ in eq.(3) are the *Mass Attenuation Coefficients* (MAC) of water and bone while $x_1(\boldsymbol{r})$, $x_2(\boldsymbol{r})$ are given bellow:

$$x_1(\boldsymbol{r}) = f_w(\boldsymbol{r}) \rho(\boldsymbol{r}) \tag{5a}$$

$$x_2(\boldsymbol{r}) = f_b(\boldsymbol{r}) \rho(\boldsymbol{r}) \tag{5b}$$

where $\rho(\boldsymbol{r})$ is mass density, $f_w(\boldsymbol{r})$ and $f_b(\boldsymbol{r})$ are the density fractions of water and bone. For the materials whose attenuation is between water and bone, the two fraction factors are both between 0 and 1. In practice, the energy based decomposition functions can be pre-simulated or pre-measured.

2.2. Multi-energy forward model

Discretized eq.(3) can be written as:

$$\boldsymbol{p}_i = a_{1i} \boldsymbol{q}_1 + a_{2i} \boldsymbol{q}_2, \; i = 1, \cdots, N_e, \tag{6}$$

[*] PhD candidate at Laboratoire d'Image, Tomographie et Traitement (LITT) and Laboratoire des signaux et systèmes (L2S), France
[†] Senior Researcher of CNRS at L2S, France
[‡] Senior Researcher at CEA, France
[§] Assistant Professor at University Paris Sud and researcher at L2S, France

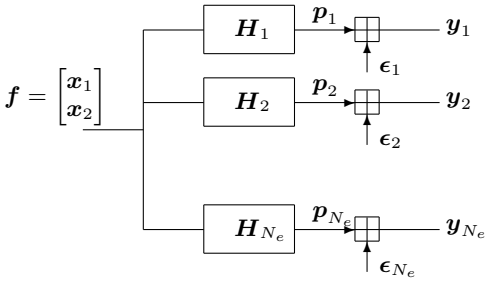

Fig. 1: *MECT forward diagram*

where N_e is the number of beam-energies at which the acquisition is done. $\boldsymbol{q}_1$ and $\boldsymbol{q}_2$ are discretized version of eq.(4) given as:

$$\boldsymbol{q}_1 = \boldsymbol{R}\boldsymbol{x}_1 \tag{7a}$$

$$\boldsymbol{q}_2 = \boldsymbol{R}\boldsymbol{x}_2 \tag{7b}$$

where $\boldsymbol{R}$ is the Radon transform matrix. Now, denote the energy selective forward matrix $\boldsymbol{H}_i$ by

$$\boldsymbol{H}_i = \begin{bmatrix} a_{1i}\boldsymbol{R} & a_{2i}\boldsymbol{R} \end{bmatrix} \tag{8}$$

and $\boldsymbol{f} = \begin{bmatrix} \boldsymbol{x}_1 & \boldsymbol{x}_2 \end{bmatrix}^T$, we have a MECT linear forward model

$$\boldsymbol{p}_i = \boldsymbol{H}_i\boldsymbol{x},\ i = 1, \cdots, N_e. \tag{9}$$

The observation $\boldsymbol{y}_i$ for the ith energy channel becomes,

$$\boldsymbol{y}_i = \boldsymbol{p}_i + \boldsymbol{\epsilon}_i,\ i = 1, \cdots N_e. \tag{10}$$

where the $\boldsymbol{\epsilon}_i$ represents all the errors and assumed to be Gaussian and its variance equals to σ_{ϵ_i}. Fig.1 shows the forward diagram.

3. INVERSION

3.1. Pre-separation inversion

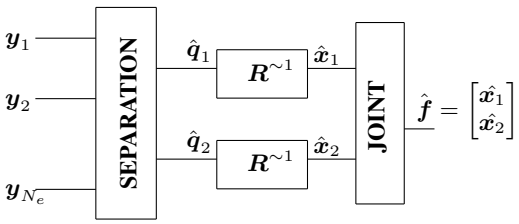

Fig. 2: *MECT pre-separation inversion diagram*

From the MECT forward model given in eq.(6), we learn that the energy selective projection can be separated into a linear combination of the sinograms for the base material fractions. In this inversion approach, first we apply a separation method onto the observation to get the estimations of the two base material projectors $\boldsymbol{q}_1$ and $\boldsymbol{q}_2$. Then Bayesian method is used to estimate the regularized inverse of the Radon transform. The diagram of this approach is shown in Fig.2, where $\boldsymbol{R}^{\sim 1}$ denotes the regular inverse of Radon transform. The separation is done by minimizing the total square error in the projection space,

$$(\hat{\boldsymbol{q}}_1, \hat{\boldsymbol{q}}_2) = \arg \min_{(\boldsymbol{q}_1, \boldsymbol{q}_2)} \left\{ \sum_i^{N_e} (a_{1i}\boldsymbol{q}_1 + a_{2i}\boldsymbol{q}_2 - \boldsymbol{y}_i)^2 \right\} \tag{11}$$

The above separation method has an analytical solution given by eq.(12),

$$\begin{bmatrix} \hat{\boldsymbol{q}}_1 & \hat{\boldsymbol{q}}_2 \end{bmatrix} = \left[(\boldsymbol{A}^T\boldsymbol{A})^{-1}\boldsymbol{A}^T \begin{bmatrix} \boldsymbol{y}_1^T \\ \boldsymbol{y}_2^T \\ \vdots \\ \boldsymbol{y}_{N_e}^T \end{bmatrix} \right]^T \tag{12}$$

where $\boldsymbol{A} = \begin{bmatrix} a_{11} & a_{21} \\ a_{12} & a_{22} \\ \vdots & \vdots \\ a_{1N_e} & a_{2N_e} \end{bmatrix}$. For the inverse of Radon transform, *Maximum A Posteriori* (MAP) estimation method is used.

$$\boldsymbol{x}_j = \arg \min_{\boldsymbol{x}_j} \left\{ ||\boldsymbol{R}\boldsymbol{x}_j - \hat{\boldsymbol{q}}_j)||^2 + \beta_j \Phi(\boldsymbol{D}\boldsymbol{x}_j) \right\},$$
$$j = 1, 2. \tag{13}$$

where $\beta_j = \sigma_{q_j}^2 / \sigma_{x_j}^2$ is the hyper-parameter who tunes the likelihood and the priori information. $||.||$ denotes the second norm. $\sigma_{x_j}^2$ is the variance of $\boldsymbol{x}_j$, $\sigma_{q_j}^2$ is the variance of $\boldsymbol{q}_j$. In practice, they are estimated by the variance of the initialization of $\boldsymbol{x}_j$ and the variance of the former estimated $\hat{\boldsymbol{q}}_j$. $\Phi(\boldsymbol{D}\boldsymbol{x})$ is the priori function. In this paper, all the priori functions are the convex Huber function which is given in eq.(14), where $\boldsymbol{D}$ denotes the spacial gradient.

$$\Phi(\boldsymbol{D}\boldsymbol{x}) = \sum_i^N \phi(\{\boldsymbol{D}\boldsymbol{x}\}_i),\ \phi(t) = \begin{cases} t^2 & \text{if } |t| > \sigma \\ \sigma(|t| - \sigma) & \text{if } |t| \leq \sigma \end{cases} \tag{14}$$

where N is the total dimension of the unknown parameter $\boldsymbol{x}$ and σ is the threshold that holds the penalties for the information of high frequency and the information of low frequency. Eq.(13) is solved iteratively.

3.2. Post-separation inversion

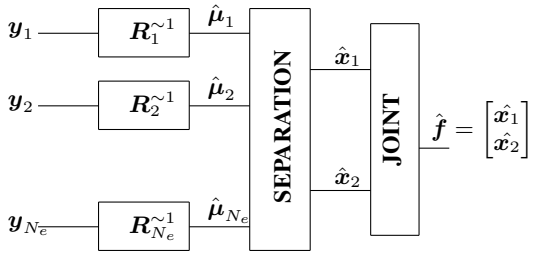

Fig. 3: *MECT post-separation inversion diagram*

Reconstruction of $\boldsymbol{x}_1$ and $\boldsymbol{x}_2$ can also be done by inversing the Radon transform first to get the LACs of the object at each energy channel. Then proper estimation method is used to get the base material fractions based on eq.(2). This approach can be shown in the diagram Fig.3.

The same as in the pre-separation approach, the inverse of the Radon transform can be done by the MAP estimation method considering LAC μ_i as the unknown parameter.

$$\hat{\boldsymbol{\mu}}_i = \arg \min_{\boldsymbol{\mu}_i} \left\{ (\boldsymbol{y}_i - \boldsymbol{R}\boldsymbol{\mu}_i)^T (\boldsymbol{y}_i - \boldsymbol{R}\boldsymbol{\mu}_i) + \beta_i \Phi(\boldsymbol{D}\boldsymbol{\mu}_i) \right\},$$
$$i = 1, 2, \cdots, N_e. \tag{15}$$

Where $\beta_i = \sigma_{\epsilon_i}/\sigma_{\mu_i}$ is the variance ratio of the noise and the attenuation at the beam energy ε_i. The base material fractions are estimated by minimizing the total square error. Similar to eq.(11), the estimation is given in eq.(16).

$$\begin{bmatrix}\hat{\boldsymbol{x}}_1 & \hat{\boldsymbol{x}}_2\end{bmatrix} = \left[(\boldsymbol{A}^T\boldsymbol{A})^{-1}\boldsymbol{A}^T\begin{bmatrix}\boldsymbol{\mu}_1^T\\ \boldsymbol{\mu}_2^T\\ \vdots\\ \boldsymbol{\mu}_{N_e}^T\end{bmatrix}\right]^T \tag{16}$$

3.3. Joint Bayesian inversion

Different from the separation approaches, the Bayesian inversion maximize the joint a posteriori distribution.

$$(\hat{\boldsymbol{x}}_1, \hat{\boldsymbol{x}}_2) = \arg\max_{(\boldsymbol{x}_1,\boldsymbol{x}_2)}\left\{\frac{p(\boldsymbol{y}/\boldsymbol{x}_1,\boldsymbol{x}_2)p(\boldsymbol{x}_1)p(\boldsymbol{x}_2)}{p(\boldsymbol{y})}\right\} \tag{17}$$

which is equal to the following optimization problem

$$(\hat{\boldsymbol{x}}_1, \hat{\boldsymbol{x}}_2) = \arg\min_{(\boldsymbol{x}_1,\boldsymbol{x}_2)}\{L(\boldsymbol{x}_1,\boldsymbol{x}_2)\} \tag{18}$$

with the cost function $L(\boldsymbol{x}_1,\boldsymbol{x}_2)$ is proportional to the negative logarithm of the joint posteriori probability, which is given as bellow

$$L(\boldsymbol{x}_1,\boldsymbol{x}_2) = L_0(\boldsymbol{x}_1,\boldsymbol{x}_2) + \lambda_1\Phi(D\boldsymbol{x}_1) + \lambda_2\Phi(D\boldsymbol{x}_2) \tag{19}$$

where $\lambda_1 = 1/\sigma_{x_1}^2, \lambda_2 = 1/\sigma_{x_2}^2$ and the likelihood term $L_0(\boldsymbol{x}_1,\boldsymbol{x}_2)$,

$$L_{0i}(\boldsymbol{x}_1,\boldsymbol{x}_2) = \sum_i^{N_e}\frac{1}{\sigma_i^2}(\boldsymbol{H}_i\begin{bmatrix}\boldsymbol{x}_1\\ \boldsymbol{x}_2\end{bmatrix} - \boldsymbol{y}_i)^T(\boldsymbol{H}_i\begin{bmatrix}\boldsymbol{x}_1\\ \boldsymbol{x}_2\end{bmatrix} - \boldsymbol{y}_i) \tag{20}$$

We see that the total cost function in eq.(19) can be seen as three parts: the total likelihood, the a priori information on $\boldsymbol{x}_1$ and the a priori information on $\boldsymbol{x}_2$.

3.4. Fast Conjugate Gradient optimization

As we see, all the above inversion approaches rely on an optimization problem, such as described in eq.(13), eq.(15) and eq.(17). Here we discuss a *Conjugate Gradient* (CG) optimization algorithm, in which an optimal descent step is used. More generally, we denote the unknown parameter as $\boldsymbol{x}$, the estimation is done by minimizing a cost function $L(\boldsymbol{x})$.

$$\hat{\boldsymbol{x}} = \arg\min_{\boldsymbol{x}}\{L(\boldsymbol{x})\} \tag{21}$$

For quadratic cost functions, the iterative CG algorithm with an optimal descent step is given bellow, where n is the iteration, $\boldsymbol{d}$ is the CG descent direction, N_{max} is the maximum iteration and δ is the gradient norm tolerance. $\boldsymbol{g}_n$ denotes the gradient of the cost function at the nth iteration $\boldsymbol{g}_n = \frac{\partial L(\boldsymbol{x})}{\partial \boldsymbol{x}}|_{\boldsymbol{x}=\boldsymbol{x}_n}$ and $\mathcal{H}_n$ is the Hessian matrix $\mathcal{H}_n = \frac{\partial^2 L(\boldsymbol{x})}{\partial \boldsymbol{x}\partial \boldsymbol{x}^T}|_{\boldsymbol{x}=\boldsymbol{x}_n}$. Their expressions for the joint cost function eq.(19) are given in the section 6.

$n=0$,	$\boldsymbol{d} = -\boldsymbol{g}_0$		
while	$n < N_{max}$	*and*	$norm(\boldsymbol{g}_n) < \delta$
do			
	α_n	=	$\frac{-\boldsymbol{g}_n^T\boldsymbol{d}}{\boldsymbol{d}^T\mathcal{H}_n\boldsymbol{d}}$
	$\boldsymbol{x}_{n+1}$	=	$\boldsymbol{x}_n + \alpha_n\boldsymbol{d}$
	β	=	$\frac{\boldsymbol{g}_{n+1}^T\boldsymbol{g}_{n+1}}{\boldsymbol{g}_n^T\boldsymbol{g}_n}$
	$\boldsymbol{d}$	=	$-\boldsymbol{g}_{n+1} + \beta\boldsymbol{d}$
	$n++$		

In the above algorithm, the descent step α_n is calculated with the objective of minimizing the cost function for the next iteration in the descent direction. This means,

$$\alpha_n = \arg\min_{\alpha}\{L(\boldsymbol{x}_n + \alpha\boldsymbol{d}_n)\} \tag{22}$$

The expression given in the CG algorithm above is the exact solution for eq.(22) while the cost function is quadratic. Even with non-quadratic cost functions, the same strategy can be used to estimate the descent step.

4. SIMULATION RESULTS

A simulated phantom (shown in Fig.4.a) of $10 \times 10\ cm^2$ numerized into 256×256 pixels is used to test our reconstruction approaches, which contains four types of materials: water(triangle), blood(square), aluminum(circle) and bone(rectangle). The water and bone fractions for a given material are estimated by minimizing the square error of the attenuation coefficients in the energy range $[10, 500]$ *keV* , given in eq.(23).

$$(\hat{f}_w, \hat{f}_b) = \arg\min_{(f_w,f_b)}\left\{\sum_i^N(a_1(\varepsilon_i)f_w\rho + a_2(\varepsilon_i)f_b\rho - \mu(\varepsilon_i))^2\right\}, \quad \varepsilon_i \in [10, 500]keV \tag{23}$$

where N is the total energy sampling number. $a_1(\varepsilon_i)$ and $a_2(\varepsilon_i)$, $i = 1, \cdots, N$ are mass attenuation coefficients of water and bone obtained from the database XCOM ([4]). $\mu(\varepsilon_i)$, $i = 1, \cdots, N$ are the LACs of the given material which can be acquired from XCOM as well for all the above four materials. ρ is the mass density of the given material. Then we can get the estimations of the two base material fractions based on eq.(5), which will be used as the original fraction references in the following comparison.

Fig.4.b shows the compositions of the phantom and their water and bone fractions coefficients. Sinograms are simulated at beam

a.phantom

N°	Material	$\hat{f}_w$	$\hat{f}_b$	ρ g/cm^3
1	water	1	0	1.00
2	blood	0.98	0.01	1.06
3	alluminium	0.17	0.75	2.70
4	bone	0	1	1.92

b.compositions

Fig. 4: *Phantom and its compostions*

energies $N_e = 4$, $\varepsilon = 40$, 60, 100, 200 *keV* with Gaussian noise of SNR(*Signal-to-Noise Ratio*) = 30 *dB* at each energy.

Fig.5 shows the simulated reconstruction results. The first column is the water fractions, the second is the bone fractions. From top to bottom, it shows the reconstructed results of pre-separation approach, the results of post-separation approach, the results of joint Bayesian approach and the profiles separately. From the profiles, we see that the joint Bayesian approach results in the best reconstructed fractions. As it maximizes the joint posteriori probability and gives different weights for the observations at different energies. To compare their reconstruction performances, *Mean Square Errors* (MSE) and the total calculation time are calculated. The Tab.1 shows

Approach	MSE of $\boldsymbol{x}_1$	MSE of $\boldsymbol{x}_2$	time (s)
Pre-separation	8.5×10^{-2}	4.6×10^{-2}	1.34×10^{3}
Post-separation	9.6×10^{-2}	5.9×10^{-2}	2.85×10^{3}
Joint-inversion	9.8×10^{-3}	8.8×10^{-3}	3.14×10^{3}

Table 1: *Performances of the reconstruction approaches*

the results. We see that joint Bayesian inversion approach gives the smallest MSE. And the pre-separation approach takes the least calculation time. Between the two separation approaches,the MSE of post-separation approach is slightly larger than the pre-separation approach. This is because in post-separation, the Radon inverse is estimated before the separation. It introduces more estimation errors as the iterative optimization can not arrive at the exact minimum. Moreover, post-separation consumes nearly two times of calculation time, which is also the ratio between the number of energies and the number of base materials. As it involves N_e estimations of the inverse Radon transform while the former only needs two. When the ratio of energy number and base material numbers increases, it multiplies the calculation time for the post-separation approach.

5. CONCLUSION

In this paper, first, a MECT forward projection model has been established based on the base material decomposition method. This forward model allows us to characterize the object as the fractions of two base materials, water and bone in our simulation. Then three inversion approaches are presented. The simulation results justified that all these reconstruction approaches can properly reconstruct a pair of base material fractions separately. And the joint Bayesian inversion approach has the best reconstruction quality comparing with the post-separation and the pre-separation approaches. However, the pre-separation approach shows its interesting point in calculation time.

For the future work, experimental data will be used to test the above MECT reconstruction approaches.

6. APPENDIX

The gradient of the MECT joint Bayesian inversion cost function $L(\boldsymbol{x}_1, \boldsymbol{x}_2)$ in eq.(19) is given,

$$\boldsymbol{g}(\boldsymbol{x}_1, \boldsymbol{x}_2) = \sum_{i=1}^{i=N_e} \frac{1}{\sigma_i^2} \boldsymbol{H}_i^T (\boldsymbol{H}_i \begin{bmatrix} \boldsymbol{x}_1 \\ \boldsymbol{x}_2 \end{bmatrix} - \boldsymbol{y}_i) + \lambda_1 \boldsymbol{D}^T \Phi'(\boldsymbol{D}\boldsymbol{x}_1) + \lambda_2 \boldsymbol{D}^T \Phi'(\boldsymbol{D}\boldsymbol{x}_2) \quad (24)$$

Its Hessian matrix

$$\mathcal{H}(\boldsymbol{x}_1, \boldsymbol{x}_2) = \begin{bmatrix} \mathcal{H}^{11} & \mathcal{H}^{12} \\ \mathcal{H}^{21} & \mathcal{H}^{22} \end{bmatrix} \quad (25)$$

with

$$\mathcal{H}^{11} = \sum_{i=1}^{i=N_e} \frac{1}{\sigma_i^2} a_{1i}^2 \boldsymbol{R}^T \boldsymbol{R} + \lambda_1 \boldsymbol{D}^T \Phi''(\boldsymbol{D}\boldsymbol{x}_1) \boldsymbol{D}$$

$$\mathcal{H}^{12} = \mathcal{H}^{21} = \sum_{i=1}^{i=N_e} \frac{1}{\sigma_i^2} a_{1i} a_{2i} \boldsymbol{R}^T \boldsymbol{R}$$

$$\mathcal{H}^{22} = \sum_{i=1}^{i=N_e} \frac{1}{\sigma_i^2} a_{2i}^2 \boldsymbol{R}^T \boldsymbol{R} + \lambda_2 \boldsymbol{D}^T \Phi''(\boldsymbol{D}\boldsymbol{x}_2) \boldsymbol{D}$$

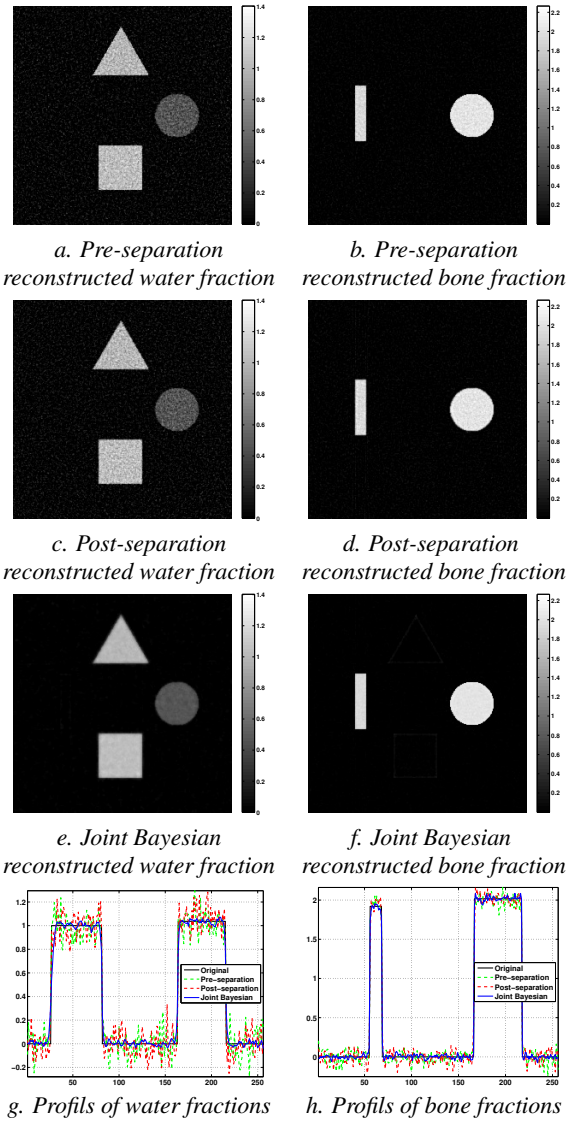

a. Pre-separation reconstructed water fraction *b. Pre-separation reconstructed bone fraction*

c. Post-separation reconstructed water fraction *d. Post-separation reconstructed bone fraction*

e. Joint Bayesian reconstructed water fraction *f. Joint Bayesian reconstructed bone fraction*

g. Profils of water fractions *h. Profils of bone fractions*

Fig. 5: *Simulation results*

7. REFERENCES

[1] Idris A. Elbakri and Jeffrey A. Fessler, "Statistical image reconstruction for polyenergetic x-ray computed tomography," *IEEE Trans. on Med. Imaging*, vol. 21, no. 2, pp. 89–99, 2002.

[2] Robert E. Alvarez and Albert Macovski, "Energy-selective reconstruction in x-ray computerized tomography," *Phys. Med. Biol.*, vol. 21, no. 5, pp. 733–744, 1976.

[3] I. A. Elbakri and J. A. Fessler, "Segmentation-free statistical image reconstruction for polyenergetic x-ray computed tomography with experimental validation," *Physics in Medicine and Biology*, vol. 48, pp. 2453–2468, 2003.

[4] J. H. Hubbell and S. M. Seltzer, "Tables of x-ray mass attenuation coefficients and mass energy-absorption coefficients," online, May 1996, http://www.nist.gov/pml/data/xraycoef/index.cfm.